Relating crevassing to non-linear strain in the floating part of Jakobshavn Isbræ, West Greenland

Paul R. PRESCOTT,[1,4] James P. KENNEALLY,[2,4] Terence J. HUGHES[3,4]

[1]*Department of Spatial Information, Science, and Engineering,* [2]*Department of Physics,* [3]*Department of Geological Sciences and*
[4]*Institute for Quaternary and Climate Studies, Bryand Global Science Center, University of Maine, Orono, ME 04469-5790, U.S.A.*
E-mail: terry.hughes@maine.edu

ABSTRACT. Jakobshavn Isbræ is a major ice stream that drains the west-central Greenland ice sheet and becomes afloat in Jakobshavn Isfjord (69° N, 49° W), where it has maintained the world's fastest-known sustained velocity and calving rate ($7 \, km \, a^{-1}$) for at least four decades. The floating portion is approximately 12 km long and 6 km wide. Surface elevations and motion vectors were determined photogrammetrically for about 500 crevasses on the floating ice, and adjacent grounded ice, using aerial photographs obtained 2 weeks apart in July 1985. Surface strain rates were computed from a mesh of 399 quadrilateral elements having velocity measurements at each corner. It is shown that heavy crevassing of floating ice invalidates the assumptions of linear strain theory that (i) surface strain in the floating ice is homogeneous in both space and time, (ii) the squares and products of strain components are nil, and (iii) first- and second-order rotation components are small compared to strain components. Therefore, strain rates and rotation rates were also computed using non-linear strain theory. The percentage difference between computed linear and non-linear second invariants of strain rate per element were greatest (mostly in the range 40–70%) where crevassing is greatest. Isopleths of strain rate parallel and transverse to flow and elevation isopleths relate crevassing to known and inferred pinning points.

INTRODUCTION

Jakobshavn Isbræ becomes afloat in Jakobshavn Isfjord at 69° N, 49° W in Disko Bugt, West Greenland (see Fig. 1). It has the fastest sustained ice velocity, moving $7 \, km \, a^{-1}$ at its terminus for a half-century (Bader, 1961; Carbonnell and Bauer, 1968; Lingle and others, 1981; Echelmeyer and others, 1992; Fahnestock and others, 1993; Fastook and others, 1995). Bader (1961) defined "ice stream" as a fast current of ice imbedded in an ice sheet, based on Jakobshavn Isbræ. Carbonnell and Bauer (1968) made the first use of aerial photogrammetry in glaciology to measure velocities of its floating portion. Lingle and others (1981) made the first measurements of tidal flexure along its grounding lines to study iceberg calving along tidal crevasses. Echelmeyer and others (1991, 1992) studied the surface morphology and mass balance, and Fastook and others (1995) photogrammetrically mapped surface elevations and velocities of $10\,000 \, km^2$ of ice converging on Jakobshavn Isfjord. Wong and others (1998) used radar sounding to map ice thicknesses over this area. Iken and others (1993) and Funk and others (1994) measured internal temperatures by thermal drilling into the main trunk of the ice stream, and modeled its dynamics where Clarke and Echelmeyer (1989) had measured ice thicknesses along seismic profiles. Echelmeyer and Harrison (1990) showed that seasonal variations of velocity across the grounding line of the main trunk were not above measurement errors, but tidal variations were, causing the rear grounding line to migrate. Reeh (1968) and Fastook and Schmidt (1982) used Jakobshavn Isbræ to study calving caused by arching of floating ice along the calving front in response to the vertical asymmetry of the

longitudinal gravitational force. Weidick and others (1990) showed that the calving front had three episodes of rapid retreat since the Last Glacial Maximum, first in Disko Bugt until 8000 years ago, then during Holocene climate warming until 5000 years ago, and in Jakobshavn Isfjord after 1850, when the Little Ice Age ended. Bindschadler (1984) and Pelto and others (1989) estimated the mass balance of the Jakobshavn ice-drainage system in Greenland.

DATA PRESENTATION

These earlier studies showed that the Jakobshavn ice drainage system was close to mass-balance equilibrium from 1964 to 1996, that Jakobshavn Isfjord continues beneath the main trunk of the ice stream for almost 100 km, that basal ice in the main trunk is sliding and is polythermal ice some 200 m thick, that supraglacial lakes in the ablation zone can drain quickly through crevasses, that crevasses prevent surface run-off of summer meltwater, that crevasses become ubiquitous as ice becomes afloat, and that the relation between crevassing and calving is complex. Our study focused on this complex relationship. We densified by six-fold the number of surface elevation and velocity measurements made by Fastook and others (1995) on floating and grounded ice at the head of Jakobshavn Isfjord, obtaining some 500 velocity vectors. These were controlled by fixed targets on the fjord sidewalls that were located by Doppler transit surveys from Earth-orbiting satellites, and triangulated to moving targets (crevasses, seracs, etc.) on the ice that were visible in aerial photographs obtained on 10 and 24 July 1985. The local geoid was
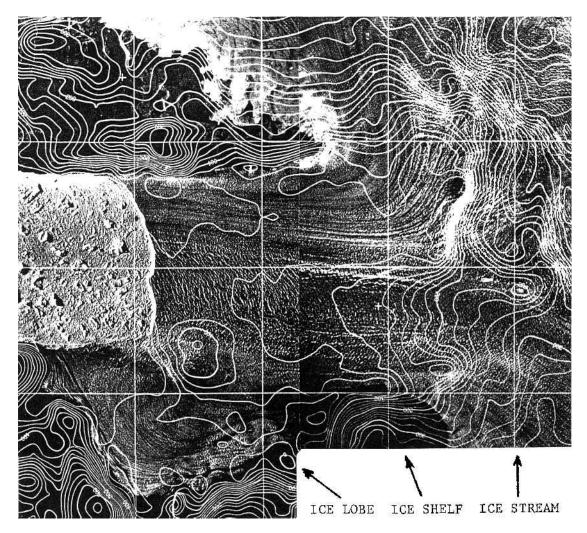
149

Fig. 1. Jakobshavn Isbræ floating in Jakobshavn Isfjord at 69° N, 49° W, West Greenland. Photo flight on 24 July 1985 by Henderson Aerial Surveys, Inc. Surface elevations were contoured at 2 m intervals by KUCERA International.

represented by an ellipsoid with data collated within a geocentric coordinate system so that our data could be easily correlated with similar data from any other Greenland ice stream. A Lambert conic projection was used for visualizing data in the map plane, with each data point accurate to within 2.0 m horizontally and 3.5 m vertically. Details of these measurement procedures are in Prescott (1995).

In addition to data collected on moving ice, elevations of ice-polished side-walls were mapped along Jakobshavn Isfjord. As seen in Figure 2, these elevations decrease to sea level down Jakobshavn Isfjord over some 35 km, and correlate with retreat of the calving front since 1850, as reported by Carbonnell and Bauer (1968) and by Weidick and others (1990). The former ice elevations show that in 1850 Jakobshavn Isbræ was grounded in Jakobshavn Isfjord for some 20 km beyond the present-day grounding line, assuming that the fjord is not deeper than 1000–1500 m below sea level over this distance, as reported by Echelmeyer and others (1991). Therefore, retreat of the calving front was accompanied by upslope ice thinning.

Surface elevations of floating and grounded ice at the head of Jakobshavn Isfjord are shown in Figure 3. The main trunk of Jakobshavn Isbræ curves into the fjord just south of a major icefall. A secondary and much shorter current of ice enters the fjord just north of the icefall. The two currents of ice meet at the base of the icefall, where several major longitudinal crevasses open and continue to the calving front, a

distance of 10 km. These crevasses are collectively called the Zipper, because they seem to connect the two currents of ice. Floating ice is about 10 m lower in elevation north of the Zipper. South of the Zipper, the thicker ice spills over the lower south fjord side-wall and forms a grounded ice lobe in compressive flow that generates concentric folds along the lobe margin, except along a small stream-fed ice-dammed lake, where a calving ice wall develops. A local ice dome 20 m higher than surrounding ice is about 3 km behind the calving front on the south side. A supraglacial lake covers thin ice at the base of the icefall just north of the Zipper, indicating that thin ice pours over a bedrock hill at the head of the fjord, to produce the icefall. Ice-surface slopes increase sharply beyond the rear grounding line of floating ice, indicating substantial ice–bed coupling.

Surface velocities of floating and grounded ice at the head of Jakobshavn Isfjord are shown in Figure 4. Velocity vectors show that flow from the main trunk of Jakobshavn Isbræ crosses the Zipper, and supplies some 80% of ice at the north–south calving front. Velocity vectors also show that much of the ice spilling over the south fjord wall from the main-trunk ice stream curves back into the fjord and calves along an east–west calving front, instead of melting on land. Therefore, longitudinal crevasses in the Zipper are opened by transverse extension as thick trunk ice pinches out thinner ice to the north and spills over the fjord wall to the south. The current of ice entering Jakobshavn Isbræ north of the icefall
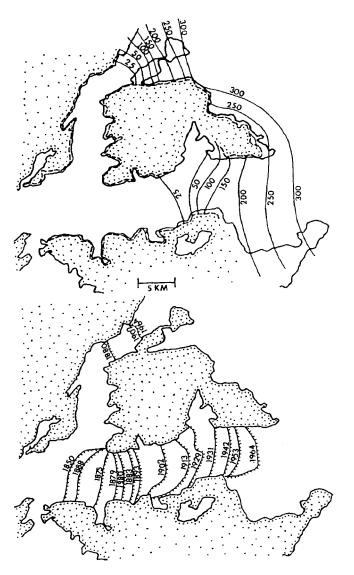
150

Fig. 2. *Thinning retreat of Jakobshavn Isbræ since the Little Ice Age in Greenland. Top: ice surface elevations in 1850 (?) based on the upper limit of glacially polished bedrock (Prescott, 1995). Bottom: retreat of the calving front, 1850–1964 (Carbonnell and Bauer, 1968).*

is not a true ice stream; rather, it is ice drawn into the fjord by faster ice in the main-trunk ice stream. This induced flow seems to generate an anticlockwise swirl of velocity vectors just below the accuracy of measurement in ice entering the fjord from the north. These ice velocities, ice velocities over the icefall, and ice velocities in the ice lobe are all small compared to the velocities in the main-trunk ice stream and of floating ice. Velocity vectors pass over, and partly around, a local ice dome just behind the south side of the calving front, indicating that the dome results from weakly grounded ice that creates ice rumples, not an ice rise. Contoured isopleths of ice velocity in Figure 5 show that ice velocity peaks at 7 km a^{-1} as it crosses the rear grounding line of the main-trunk ice stream, slows slightly, and peaks again at 7 km a^{-1} near the calving front. This suggests other partial grounding sites in the fjord in addition to the ice rumples. Strong lateral velocity gradients and shear crevasses rotated to longitudinal orientations along both fjord side-walls do not extend into the main-trunk flow of floating ice. This indicates partial lateral uncoupling of ice from fjord side-walls, possibly due to tidal flexure concentrated along these crevasses, as analyzed by Lingle and others (1981).

DATA ANALYSIS

The major assumption controlling analysis of our data is that rotation rates and strain rates have comparable magnitudes in heavily crevassed floating ice having horizontal dimensions an order of magnitude greater than the vertical thickness (Truesdale, 1952). These are the conditions for non-linear strain (Love, 1927, p. 59; Novozhilov, 1953; Sokolnikoff, 1956, p. 28). Displacements u_i of points initially at positions x_i give new positions:

$$\xi_i = x_i + u_i . \qquad (1)$$

Differentiating for infinitesimal displacements:

$$\mathrm{d}\xi_i = \big(\delta_{ij} + u_{i,j}\big)\mathrm{d}x_j = \big(\delta_{ij} + e_{ij} + \omega_{ij}\big)\mathrm{d}x_j , \qquad (2)$$

where δ_{ij} is the Kronecker delta, such that $\delta_{ij} = 1$ for longitudinal displacements $i = j$ and $\delta_{ij} = 0$ for transverse
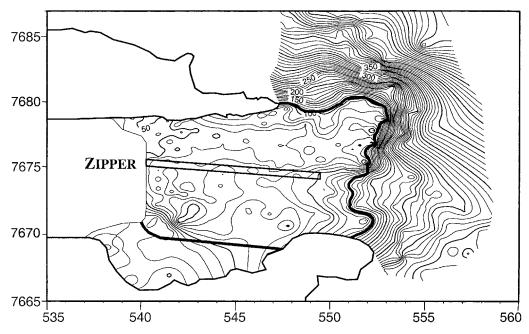

Fig. 3. *Surface elevations on Jakobshavn Isbræ contoured at 5 m intervals above the OSU91A1F geoid (Prescott, 1995). The bold line is the tentative grounding line. The long rectangle encloses crevasses in the Zipper.*
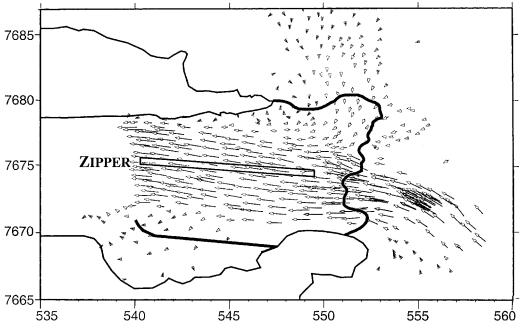
151

Fig. 4. Surface velocity vectors of floating and grounded ice at the head of Jakobshavn Isfjord (Prescott, 1995). Velocities range over three orders of magnitude, so slow velocities are only points inside arrowheads.

displacements $i \neq j$, $u_{i,j} = \partial u_i / \partial x_j$ when $i, j = x_1, x_2, x_3$ and $u_{i,j} = \partial u_i / \partial j$ when $i, j = x, y, z$, $e_{ij} = 1/2(u_{i,j} + u_{j,i})$ are linear strain components, and $\omega_{ij} = 1/2(u_{i,j} - u_{j,i})$ are angular rotation components.

Forming the squares of the distances between the points M and N before deformation and between M′ and N′ after deformation gives the following:

$$ds^2 = dx_i dx_i \quad \text{for} \quad |\overrightarrow{MN}|^2$$
$$ds'^2 = d\xi_i d\xi_i \quad \text{for} \quad |\overrightarrow{M'N'}|^2 \,. \tag{3}$$

Taking the difference of the distance squares and using Equation (1) produces:

$$ds'^2 - ds^2 = 2\varepsilon_{ij} \, dx_i \, dx_j \,, \tag{4}$$

where ε_{ij} are the non-linear (also known as the Cauchy–Green or finite) strain components defined by:

$$\varepsilon_{ij} = \frac{1}{2}(u_{i,j} + u_{j,i} + u_{k,i} u_{k,j}) \,. \tag{5}$$

Using Equation (2), Equation (4) can also be defined in terms of the linear strains:

$$ds'^2 - ds^2 = 2\left\{ e_{ij} + \frac{1}{2} \left[(e_{ik} - \omega_{ik})(e_{jk} - \omega_{jk}) \right] \right\} dx_i \, dx_j \,. \tag{6}$$

Thus the relation between the linear and non-linear strain components is:

$$\varepsilon_{ij} = e_{ij} + \frac{1}{2} \left[(e_{ik} - \omega_{ik})(e_{jk} - \omega_{jk}) \right] \,. \tag{7}$$

From Equation (7) it can be seen that the non-linear strain includes the second-order products between the linear strains and rotations.
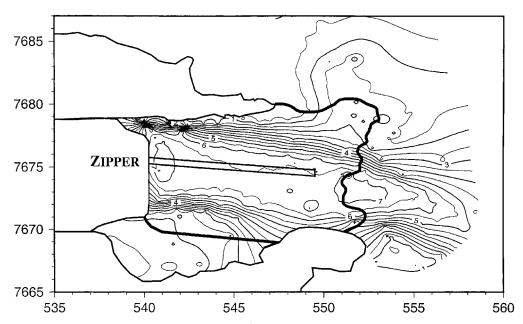

Fig. 5. Isopleths of surface velocities contoured at 0.5 km a^{-1} intervals at the head of Jakobshavn Isfjord (Prescott, 1995).
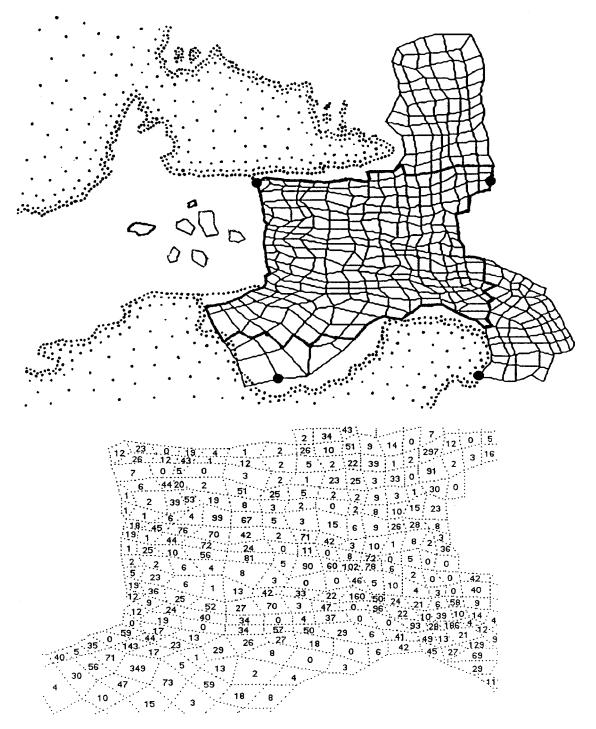
152

Fig. 6. A mesh of quadrilateral elements created from point locations on Jakobshavn Isbræ. Top: the complete mesh. Bottom: the part of the mesh inside the bold border showing the percentage difference between computed linear and non-linear strain rates for each element.

Principal strain rates give the largest values of the normal strain-rate components. Assuming that surface strain rates do not vary through the floating ice thickness, the linear and non-linear principal strain rates were computed using the standard relation (Chou and Pagano, 1967, p. 10). In terms of east–west and north–south axes x and y, respectively parallel and transverse to Jakobshavn Isfjord, the maximum non-linear normal strain rates are:

$$\dot{\varepsilon}_{11} = \frac{\dot{\varepsilon}_{xx} + \dot{\varepsilon}_{yy}}{2} + \sqrt{\frac{1}{4}\left(\dot{\varepsilon}_{xx} + \dot{\varepsilon}_{yy}\right)^2 + \dot{\varepsilon}_{xy}^2} \qquad (8a)$$

$$\dot{\varepsilon}_{22} = \frac{\dot{\varepsilon}_{xx} + \dot{\varepsilon}_{yy}}{2} - \sqrt{\frac{1}{4}\left(\dot{\varepsilon}_{xx} + \dot{\varepsilon}_{yy}\right)^2 + \dot{\varepsilon}_{xy}^2}. \qquad (8b)$$

Instead of computing the rotational angle associated with the principal strain rates, which is coordinate-system dependent, the value of maximum non-linear shear strain rate was computed:

$$\dot{\varepsilon}_{12}^{\max} = \sqrt{\frac{1}{4}\left(\dot{\varepsilon}_{xx} + \dot{\varepsilon}_{yy}\right)^2 + \dot{\varepsilon}_{xy}^2}. \qquad (9)$$

For linear strain rates, replace $\dot{\varepsilon}_{ij}$ with $\dot{e}_{ij}$ in Equations (8) and (9). From the non-linear adjustment, the standard deviations for the velocity gradients were computed and then using the law of variance–covariance propagation (e.g. Leick and Humphrey, 1981, p. 102), the standard deviations for the principal strain rates and maximum shear strain rate were computed. The relation between the standard deviations for the velocity gradients and those for the principal strain rates is:

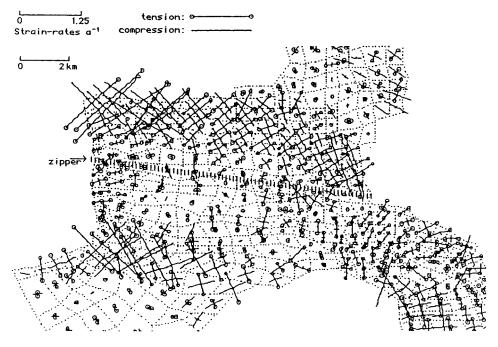$$\Sigma_i^y = G_i \, \Sigma_{ij}^x \, G_j \,, \qquad (10)$$

153

Fig. 7. Non-linear principal strain rates computed for each element of the mesh generated from point measurements of surface velocity on Jakobshavn Isbræ (Prescott, 1995).

where Σ_{ij}^x is the variance–covariance matrix of $u_{i,j}$, Σ_i^y is the square of the standard deviations for the principal strains, and G_i is the vector describing the linear relationship between Σ_{ij}^x and Σ_i^y. The subscripts i and j range over the number of parameters in Σ^y and in the variance–covariance matrix, respectively. See Prescott (1995) for further details.

Figure 6 shows a mesh of 399 quadrilateral elements that was created from the measured point locations on Jakobshavn Isbræ to compute the linear and non-linear strain rates. For the majority of the elements, the measured displacements served as the corners.

As discussed in detail by Prescott (1995), the data were made more robust using the following technique. The error estimates for each observation are changed after each iteration so that they are proportional to the computed residuals (Leick and Humphrey, 1981). In this case, the weights were set to the inverse of the square of the residuals. This procedure produced the percentage errors of the minimum strain rate, the minimum shear rate and the second invariant (7%, 8% and 17%).

A comparison was made between the linear and non-linear strain rates by calculating percentage differences for the strain rates in the local coordinate system, the principal strain rates and maximum shear rate, and the second invariant. Although the majority of the principal strain rates and maximum shear rates agree to within 10%, there still are about one-third of the data that differ by $>20\%$. The difference between the second invariants is somewhat worse, with less than half of the data agreeing to within 10%, and 38% differing by $>20\%$. For the local coordinate-system strain-rate components, the comparison is worse. The most noticeable difference is in the transverse y component, where 30% of the data differ by $>50\%$. This larger difference is probably due to the x-coordinate axis approximately corresponding to the flow direction, so that the magnitudes of the y-component strain rates are much smaller. However, based on the statistical methods outlined above, the y-component strain rates should be considered valid.

In general, it appears that the maximum shear rate and the local shear rate give the best agreement between the linear and non-linear forms. If this is indeed true, then certain inferences can be drawn about the data. Rewriting Equation (7) for the two-dimensional case gives:

$$\varepsilon_{xx} = e_{xx} + \frac{1}{2}\left[e_{xx}^2 + \left(e_{xy} - \omega_{xy}\right)^2\right] \tag{11a}$$

$$\varepsilon_{yy} = e_{yy} + \frac{1}{2}\left[e_{yy}^2 + \left(e_{xy} + \omega_{xy}\right)^2\right] \tag{11b}$$

$$\varepsilon_{xy} = e_{xy} + e_{xx}\left(e_{xy} + \omega_{xy}\right) + e_{yy}\left(e_{xy} - \omega_{xy}\right). \tag{11c}$$

Strain rates are obtained from the strains in Equations (11) by dividing the strains by the time during which strains were measured. Equations (11) then show that the invalidity of the linear form for the normal strain rates could be due to the square of the normal strain rate not being small compared to unity, and/or the square of the rotation rate $\dot{\omega}_{ij}$ not being small compared to the normal strain-rate component.

RESULTS

The data analysis showed that non-linear strain theory was preferable to linear strain theory in accounting for deformation of the floating part of Jakobshavn Isbræ. Figure 6 shows the percentage difference per element between the second invariants of strain rate, $\dot{e} = (\frac{1}{2}\dot{e}_{ij}\dot{e}_{ij})^{1/2}$ for linear strain rates and $\dot{\varepsilon} = (\frac{1}{2}\dot{\varepsilon}_{ij}\dot{\varepsilon}_{ij})^{1/2}$ for non-linear strain rates. These differences are greatest where crevassing is greatest, namely, along the Zipper and in the lateral shear zones, indicating a concentration of rotated elements where ice is most fractured.

Figure 7 shows non-linear principal strain rates obtained from the mesh of quadrilateral elements in Figure 6. Since corners of elements typically coincide with corners of prominent crevasses, each element may be a discrete parcel of ice within which deformation may be largely homogeneous, with inhomogenities concentrated between elements. Principal strain rates confirm transverse extension across the Zipper as the explanation for opening longitudinal crevasses along
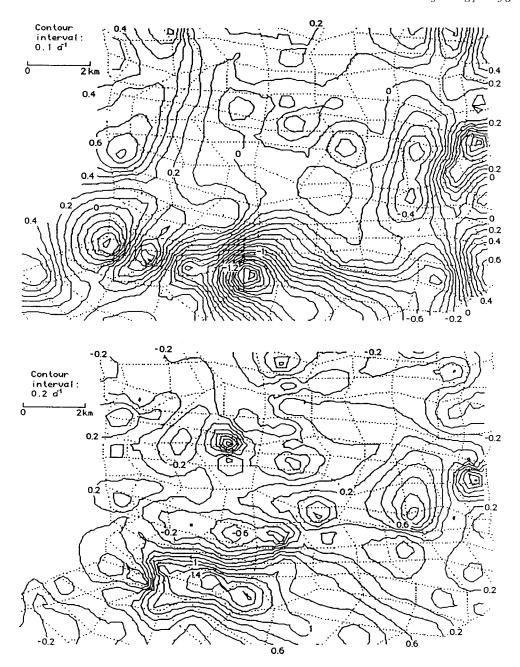
154

Fig. 8. Isopleths contoured at $0.1\,a^{-1}$ intervals for non-linear strain rates $\dot{\varepsilon}_{xx}$ (top) and $\dot{\varepsilon}_{yy}$ (bottom) respectively parallel and transverse to ice-flow vectors in Figure 4. Also shown is the portion of the finite-element mesh in Figure 5 that was used in these calculations.

the Zipper, and confirm sub-longitudinal compression in ice approaching the ice rumples as an explanation for little velocity change from the rear grounding line to the calving front. Simple shear, consisting of equal parts pure shear and rigid rotation, dominates in floating ice north of the Zipper and between the south grounded ice lobe and the main floating trunk of the ice stream. Pure linear extension, coinciding with release of the largest icebergs, occurs between the Zipper and the ice rumples.

Figure 8 shows isopleth contours for non-linear strain rates $\dot{\varepsilon}_{xx}$ parallel to flow and $\dot{\varepsilon}_{yy}$ transverse to flow. These show strong extending and compressive flow beyond and behind the ice rumples, respectively, combined with transverse extension behind the ice rumples. This indicates a tendency for ice to flow around the ice rumples as well as across the ice rumples. Therefore ice grounding beneath the ice rumples is firm enough to give the ice rumples some characteristics of an ice rise. Closed strain-rate isopleths scattered over the floating ice

give hints of partial grounding elsewhere. Longitudinal strain rates are compressive below the icefall, tensile near the calving front, and close to zero in between. Transverse strain rates become increasingly tensile toward the icefall. This is compatible with the general absence of large transverse crevasses and the prominent longitudinal crevasses (the Zipper) in this region. The near-zero longitudinal strain rate ($\dot{\varepsilon}_{xx} \approx 0$) and the average extending transverse strain rate ($\dot{\varepsilon}_{yy} \approx 0.2\,a^{-1}$) over most of the region from the grounding line to the calving front allows a calculation of ice thinning over this 10 km distance due to ice melting on the top and bottom surfaces. Taking 50 m as the elevation change in Figure 3 and 6.8 km a^{-1} as the ice velocity in Figure 4, with ice thickness as 9.2 times ice elevation (Echelmeyer and others, 1991), and taking $\dot{\varepsilon}_{zz} = -(\dot{\varepsilon}_{xx} + \dot{\varepsilon}_{yy}) = -0.2\,a^{-1}$ as the vertical thinning creep rate, ice 1012 m thick (110 m high) at the rear grounding line thins by 202 m a^{-1} and is 300 m thinner at the calving front due to creep thinning. The actual thinning is 460 m, which

155

requires a net melting rate of $109 \, \mathrm{m \, a^{-1}}$. This compares with $44 \, \mathrm{m \, a^{-1}}$ beneath the floating part of Pine Island Glacier in Antarctica (Rignot and Jacobs, 2002).

DISCUSSION

Non-linear strain rates are concentrated in the most heavily crevassed ice, indicating that the assumptions of continuum mechanics break down in these regions. Longitudinal crevasses in the Zipper are opened by transverse extension. Floating ice moves with little longitudinal deformation between the icefall and the calving front. Ice north of the icefall is drawn into Jakobshavn Isfjord by fast flow in the main trunk of Jakobshavn Isbræ. Flow from the main trunk occurs along 80% of the north–south calving front. The position of the calving front is stabilized by ice rumples south of the Zipper, and perhaps by other partial grounding elsewhere. Tidal crevasses and rotated shear crevasses significantly decouple ice in the main trunk from the fjord sidewalls. Large tabular icebergs are released primarily along the narrow zone of pure longitudinal extension between the Zipper and the ice rumples. The size of tabular icebergs may be determined by the spacing of large transverse crevasses that open as the main-trunk ice stream crosses the rear grounding line, where ice accelerates and is bent by tidal flexure, as these crevasses are transported passively to the calving front. Melting of floating ice on the top and bottom surfaces is an important ablation process. In the main trunk of floating ice, 10 km long, 3 km wide, and averaging 550 m thick along the calving front, $3.3 \, \mathrm{km^3 \, a^{-1}}$ of ice are lost by melting, and $11.2 \, \mathrm{km^3 \, a^{-1}}$ are lost by calving.

ACKNOWLEDGEMENTS

REFERENCES

Bader, H. 1961. The Greenland ice sheet. *CRREL Monogr.* I-B2.

Bindschadler, R. A. 1984. Jacobshavns Glacier drainage basin: a balance assessment. *J. Geophys. Res.*, **89**(C2), 2066–2072.

Carbonnell, M. and A. Bauer. 1968. Exploitation des couvertures photographiques aériennes répétées du front des glaciers vêlant dans Disko Bugt et Umanak Fjord, juin–juillet, 1964. *Medd. Grønl.*, **173**(5).

Chou, P. C. and N. J. Pagano. 1967. *Elasticity-tensor, dyadic, and engineering approaches*. New York, Dover. (Reprint 1992.)

Clarke, T. S. and K. Echelmeyer. 1989. High resolution seismic reflection profiles across Jakobshavns ice stream, Greenland. [Abstract.] *Eos*, **70**(43), 1080.

Echelmeyer, K. and W. D. Harrison. 1990. Jakobshavns Isbræ, West Greenland: seasonal variations in velocity — or lack thereof. *J. Glaciol.*, **36**(122), 82–88.

Echelmeyer, K., T. S. Clarke and W. D. Harrison. 1991. Surficial glaciology of Jakobshavns Isbræ, West Greenland: Part I. Surface morphology. *J. Glaciol.*, **37**(127), 368–382.

Echelmeyer, K., W. D. Harrison, T. S. Clarke and C. Benson. 1992. Surficial glaciology of Jakobshavns Isbræ, West Greenland: Part II. Ablation, accumulation and temperature. *J. Glaciol.*, **38**(128), 169–181.

Fahnestock, M., R. Bindschadler, R. Kwok and K. Jezek. 1993. Greenland ice sheet surface properties and ice dynamics from ERS-1 SAR imagery. *Science*, **262**(5139), 1530–1534.

Fastook, J. L. and W. F. Schmidt. 1982. Finite element analysis of calving from ice fronts. *Ann. Glaciol.*, **3**, 103–106.

Fastook, J. L., H. H. Brecher and T. J. Hughes. 1995. Derived bedrock elevations, strain rates and stresses from measured surface elevations and velocities: Jakobshavns Isbræ, Greenland. *J. Glaciol.*, **41**(137), 161–173.

Funk, M., K. Echelmeyer and A. Iken. 1994. Mechanisms of fast flow in Jakobshavns Isbræ, West Greenland: Part II. Modeling of englacial temperatures. *J. Glaciol.*, **40**(136), 569–585.

Iken, A., K. Echelmeyer, W. Harrison and M. Funk. 1993. Mechanisms of fast flow in Jakobshavns Isbræ, West Greenland: Part I. Measurements of temperature and water level in deep boreholes. *J. Glaciol.*, **39**(131), 15–25.

Leick, A. and D. Humphrey. 1981. *Adjustments with examples*. Orono, ME, University of Maine, Department of Survey Engineering. (Report 27.)

Lingle, C. S., T. J. Hughes and R. C. Kollmeyer. 1981. Tidal flexure of Jakobshavns glacier, West Greenland. *J. Geophys. Res.*, **86**(B5), 3960–3968.

Love, A. E. H. 1927. *A treatise on the mathematical theory of elasticity. Fourth edition.* New York, Dover.

Novozhilov, V. V. 1953. *Foundations of the nonlinear theory of elasticity*. Rochester, NY, Graylock. (Translated by F. Bagemihl, H. Komm and W. Seidel.)

Pelto, M. S., T. J. Hughes and H. H. Brecher. 1989. Equilibrium state of Jakobshavns Isbræ, West Greenland. *Ann. Glaciol.*, **12**, 127–131.

Prescott, P. R. 1995. Photogrammetric examination of the calving dynamics of Jakobshavns Isbræ, Greenland. (Ph.D. thesis, University of Maine.)

Reeh, N. 1968. On the calving of ice from floating glaciers and ice shelves. *J. Glaciol.*, **7**(50), 215–232.

Rignot, E. and S. S. Jacobs. 2002. Rapid bottom melting widespread near Antarctic ice sheet grounding lines. *Science*, **296**(5575), 2020–2023.

Sokolnikoff, I. S. 1956. *Mathematics theory of elasticity. Second edition.* New York, McGraw-Hill.

Truesdale, C. 1952. The mechanical foundations of elasticity and fluid dynamics. *J. Rational Mech. Anal.*, **2**(2 and 3), 125–300 and 593–616.

Weidick, A., H. Oerter, N. Reeh, H. H. Thomsen and L. Thoring. 1990. The recession of inland ice margin during the Holocene climatic optimum on the Jacobshavn Isfjord area of west Greenland. *Palaeogeogr., Palaeoclimatol., Palaeoecol., Global and Planetary Change Section*, **82**(3–4), 389–399.

Wong, Y. C. *and 6 others*. 1998. *Radar thickness measurements over the Greenland ice sheet: 1997 results*. Lawrence, KS, University of Kansas Center for Research Inc. Radar Systems and Remote Sensing Laboratory. (Technical Report 10470-7.)